The chromatin reader PHF6 at the crossroad of the replication stress and DNA damage responses in neuroblastoma through interaction with RRM2

Lisa Depestel[1,2], Ellen Sanders[1,2], Sarah-Lee Bekaert[1,2], Carolien Van Damme[1,2,3], Aline Eggermont[1,2], Siebe Loontiens[1,2], Laurentijn Tilleman[4], Filip Van Nieuwerburgh[4], Jan Willem Bek[1,2], Louis Delhaye[1,2,3], Pieter Van Vlierberghe[1,2], Sven Eyckerman[1,2,3], Kaat Durinck[1,2*]

[1] Department of Biomolecular Medicine, Ghent University, Ghent, Belgium.
[2] Cancer Research Institute Ghent (CRIG), Ghent, Belgium.
[3] VIB-UGent Center for Medical Biotechnology, Ghent University, Ghent, Belgium.
[4] NXTGNT, Faculty of Pharmaceutical Sciences, Ghent University, Ghent, Belgium.

*Corresponding author: prof. dr. Durinck Kaat
Department for Biomolecular Medicine, Ghent University, Medical Research Building (MRB1), Corneel Heymanslaan 10, B-9000 Ghent, Belgium
Phone: +3293322451, Fax: +3293326549, E-mail: kaat.durinck@ugent.be

Abstract

The ′plant homeodomain zinc finger protein 6′ (PHF6) is affected by germline mutations in patients with cognitive disabilities and somatic mutations in acute T-cell leukemia (T-ALL). We and others previously obtained evidence for a key role of PHF6 in hematopoietic precursor cell self-renewal capacity and lineage commitment during differentiation, while recent work revealed a role in non-homologous end joining and G2 checkpoint recovery. In this study, we identified the ribonucleotide reductase subunit M2 (RRM2), as a novel PHF6 interacting protein by immunoprecipitation coupled mass spectrometry. We confirmed the PHF6-RRM2 interaction in different normal and malignant cellular background and mapped the interaction interface towards the first PHD domain of PHF6 through NanoBRET™ based deletion mapping. We also demonstrated that PHF6 knockdown in neuroblastoma cells causes increased replicative stress and DNA damage. Furthermore, we show binding of PHF6 to the DNA-damage associated H3K56ac histone mark. In view of our recent finding of RRM2 as a MYCN co-dependency and target for synergistic CHK1 inhibition in neuroblastoma, we performed CUT&RUN mapping of H3K56ac and PHF6 genome-wide binding sites in neuroblastoma cells and next to a significant overlap of the two, we also found evidence for a functional crosstalk with established core regulatory circuitry transcription factors. Our data suggest that PHF6 is a component of the earlier proposed ‘replitase’, implicated in active regulation of RRM2 function during replication and DNA repair.

Introduction

While genomic instability is a *bona fide* cancer initiating process[1], malignant cells also need to acquire adaptations to cope with accumulating DNA damage. This enables cancer cells to cope with increased stalling and collapse of replication forks, a phenomenon called replicative stress which negatively impacts on proliferation. Evidence is emerging that cancer cells can adopt a so-called ‘addictive cellular state of replication stress resistance’. As cancer cells strongly depend on such adaptations, they can serve as targetable vulnerabilities[2,3]. Previous studies have shown a functional connection between replicative stress resistance, DNA

damage repair and nucleosome remodeling in control of chromatin dynamics[4,5]. Recently, it was shown that the chromatin reader 'plant homeodomain zinc finger protein 6' (PHF6), an interactor of various nucleosome remodeling complexes including NuRD[6], PAF1[7] and SWI/SNF[8], is involved in replication fork restart and DNA damage repair, but its exact mode-of-action in these processes still remains elusive[8,9].

The PHF6 protein structure contains four nuclear/nucleolar localization signals as well as two nearly identical extended PHD-like zinc finger domains (ePHD). These ePHD domains putatively mediate protein-protein interactions and are involved in the interaction with histone post-translational modifications to control gene expression[10,11]. Mutations in *PHF6* were first described in the Börjeson-Forssman-Lehman syndrome (BFLS), an X-linked mental retardation and cancer predisposition syndrome[12,13]. Later, *PHF6* mutations were also identified in patients with the Coffin-Siris syndrome[14], which show overlapping phenotypic features with BFSL and in which mainly mutations in several components of the SWI/SNF chromatin remodeling complex were previously reported. These observations converge towards a role of PHF6 in neural development, which is further supported by the high expression of *Phf6* in the developing central nervous system in mice[15].

Previous work, including contributions from our team, pointed to a key role for PHF6 as a tumor suppressor in a specific subtype of T-cell acute lymphoblastic leukemia (T-ALL)[16]. Later, mutations were also found in amongst others AML[17], CML[18], mixed phenotype acute leukemia (MPAL)[19] and hepatocellular carcinoma[20]. Interestingly, Huether and colleagues[21] showed that *PHF6* is one of the most frequently somatically mutated genes in pediatric cancers. However, according to another study[22], PHF6 is overexpressed in many cancer types such as breast and colorectal cancers, as well as in T-ALL without PHF6 mutations. However, in bladder cancer[23] and endometrial carcinoma[24], high expression of PHF6 have been correlated to a favorable patient outcome. In this respect, PHF6 may act as either tumor suppressor or tumor promoting gene in a lineage dependent manner.

In this study, we performed a comprehensive functional analysis of PHF6 in neuroblastoma cells through an integrative landscaping of its interactome, mapping of genome-wide binding sites and profiling of the transcriptional signatures following perturbed PHF6 expression.

Results

Identification of RRM2 as a functional PHF6 interaction partner

In follow-up of our previous work on PHF6 in the context of T-ALL[16,25], we aimed to further elucidate the functional role of PHF6 by a detailed dissection of its interactome. To this end, we performed immunoprecipitation coupled mass spectrometry (IP-MS) in HEK293T cells using endogenous PHF6 as bait, and identified the ribonucleotide reductase subunit M2 (RRM2) as top-ranked PHF6 interaction partner (**Figure 1A**). Interestingly, we recently described RRM2 as a novel copy number driven MYCN co-dependency and synergistic drug target with CHK1 in neuroblastoma, a childhood tumor arising from malignant transformation of immature sympathoblasts of the peripheral sympathetic nervous system[26,27]. Previous studies have shown that RRM2 is part of the ribonucleotide reductase complex (RNR), the rate-limiting enzyme complex involved in the synthesis of dNTPs and involved in replication, DNA damage and replicative stress responses[28]. Given that previous studies already anticipated a functional role for PHF6 in control of replication stress and DNA damage repair[8,9], we investigated whether PHF6 also interacts with RRM2 in neuroblastoma cell lines. IP-MS

experiments in CLB-GA, IMR-32, SK-N-BE(2)-C and SH-SY5Y cell lines, confirmed consistent interaction of PHF6 with RRM2 (**Figure 1B and S1**). Furthermore, we also validated the interaction in ALL-SIL (T-ALL), HCT116 (colorectal) and RPE (retinal pigmented epithelial) cell lines (**Figure S1**), showing robustness and a broad functionality of the PHF6-RRM2 interaction. Gene Ontology (GO) analysis for the PHF6 interactor hit list (FDR < 0.05) using ENRICHR[29] and ConsensusPathDB[30] tools, showed enrichment for proteins involved in ribosomal RNA processing, cell cycle regulation, DNA repair and HDAC1/2 mediated signaling events, in accordance with previously proposed functionalities for PHF6[31]. Interestingly, also proteins involved in nuclear transport of proteins and mature mRNA, as well as SUMOylation were enriched (**Figure 1C and 1D**). These observations led us to hypothesize that PHF6 is involved in the shuttling of RRM2 from the cytoplasm to the nucleus upon DNA damage and/or replicative stress.

PHF6 binds to RRM2 through its first PHD domain.

Endogenous co-immunoprecipitation (co-IP) followed by immunoblotting for RRM2 and PHF6 in HEK293T and IMR-32 neuroblastoma cells using PHF6 as bait confirmed the protein-protein interaction of PHF6 with RRM2 as seen by IP-MS (**Figure 2A**). Next, we used NanoBRET™[32] as orthogonal method to further investigate the PHF6-RRM2 interaction (**Figure 2B**). In brief, plasmids with N-terminal fusion of the NanoLuc® luciferase to PHF6 (Nluc-PHF6) and a C-terminal fusion of the HaloTag® to RRM2 (RRM2-HT), were co-transfected in HEK293T cells and resulted in the highest BRET ratios (**Figure S2A**), which were not significantly dependent on the amount of transfected plasmids (**Figure 2C**). The donor saturation assay curve of Nluc-PHF6 and RRM2-HT reaches hyperbolic saturation (**Figure 2D**), confirming the specificity of the interaction. The protein structure of PHF6 is characterized by two zinc finger domains called ZaP (zink knuckle, atypical PHD) domains and four localization signals for the nucleus and nucleoli. Since this atypical PHD domain is unstable in solution, the N-terminal pre-PHD domain was proposed to stabilize the PHD domains, hence, they are referred to as enhanced PHD (ePHD) domains (see ***figure 2E**, full length PHF6)*[33]. To identify the domain(s)/region(s) of PHF6 important for the interaction with RRM2, we generated a series of deletion constructs of PHF6 that were also N-terminally fused to the Nluc donor protein (**Figure 2E**). To validate our experimental set-up, we confirmed fusion protein expression from all transfected constructs (**Figure 2F**). The fragments that did not contain the first PHD domain (Fr1, Fr7 and Fr8) resulted in lower BRET ratios, except for fragment 6, which comprises the second PHD domain only. Moreover, fragments of the first PHD domain alone (Fr11) or together with the NLS following this domain (Fr10), show approximately the same BRET ratios as full length PHF6, suggesting that PHF6 interacts with RRM2 through its first PHD domain (**Figure 2E**). Previous studies indicated that the two zinc fingers of PHF6 are nearly identical[6], and indeed overlap between the deletion Fragment 6 (containing only the second PHD domain), and Fragment 10 (containing only the first PHD) showed high sequence similarity (**Figure S2B**). We postulate that, given this high protein sequence similarity, RRM2 can also bind to the second PHD domain, only if it is not structurally hindered by the pre-PHD2 domain, as is the case in Fragment 7 and Fragment 8. Since previous studies revealed that the second PHD domain of PHF6 can bind dsDNA *in vitro*[33], we propose that the first PHD domain of PHF6 can guide RRM2 in close proximity to DNA for replication/repair through its second PHD domain, potentially as part of the previously proposed "replitase" complex[34,35].

PHF6 is associated with high-risk neuroblastoma

Although PHF6 was first identified as a tumor suppressor in T-ALL[16] and AML[16,17], there is growing evidence for a more tumor promoting role of PHF6 in other cancer types. First, *PHF6* was shown to be overexpressed in many tumor entities such as breast and colorectal cancers[22]. Second, across a wide panel of tumor cell lines (CCLE database), leukemias without PHF6 loss as well as neuroblastoma cell lines show the highest PHF6 expression in a pan-cancer analysis (**Figure 3A**). Third, *Phf6* expression is significantly upregulated during TH-MYCN driven neuroblastoma tumor formation compared to the expression in ganglia from wildtype mice[36] ($p = 2.43 \times 10^{-6}$) (**Figure 3B**). Fourth, high *PHF6* expression in neuroblastoma patients correlate to poor prognosis in terms of event free and overall survival ($p = 3.5e-6$ and $p = 1.5e-7$ respectively) (**Figure 3C**). Moreover, PHF6 expression is higher in high-risk stage 4 classified neuroblastoma patients and in *MYCN*-amplified cases (**Figure 3D**). These observations converge towards a putative tumor promoting role for PHF6 in neuroblastoma. It is known that high-risk neuroblastoma genomes, while having a low mutational load are marked by highly recurrent DNA copy number alterations, including 2p and 17q gains[37]. However, no recurrent gains encompassing the *PHF6* locus on the X-chromosome have been identified in high-risk neuroblastoma patient data[38]. Interestingly, a single mutation in *PHF6* was identified (rs1556013242: c.119C>A (p.Ala40Glu) in neuroblastoma[39], although, due to lack of functional data on the implications of this variant thus far, it was classified as a variant of unknown significance (VUS). To further investigate a putative role for PHF6 as dependency gene, we tested the phenotypic and molecular effects of PHF6 depletion as well as landscape the PHF6 genome-wide binding sites in neuroblastoma cells.

Knockdown of PHF6 in neuroblastoma cell lines leads to increased replication stress and DNA damage

To evaluate the phenotypic and molecular effects of PHF6 depletion in neuroblastoma cell lines, we performed siRNA-mediated knockdown of *PHF6* in CLB-GA, SH-SY5Y, SK-N-BE(2)-C and IMR-32, and validated the knockdown through RT-qPCR (**Figure 4A**) and immunoblotting (**Figure 4B**). As previously described in *in vitro* B-ALL cell lines[40], PHF6 downregulation had no significant effect on proliferation of neuroblastoma cell lines (**Figure 4C**). PHF6 is an important factor in fork restart after DNA damage[9] and thus possibly also important in relieving replicative stress. Interestingly, pCHK1^{S345} levels were elevated upon knockdown of PHF6, as well as pRPA32 and γH2AX levels, indicative of replicative stress induction (**Figure 4D**). Previous studies reported CHK1 as a synthetic lethal target in MYCN-amplified neuroblastoma, and neuroblastoma was ranked as the most sensitive pediatric cancer for CHK1 inhibition using prexasertib[41]. Therefore, we scored publicly available gene signatures related to prexasertib sensitivity and resistance in a large cohort of primary neuroblastomas (GSE62564)[42], revealing that low PHF6 expression correlates to prexasertib resistance, while high expression levels are correlated to sensitivity for prexasertib treatment indicating high ATR-CHK1 dependency (**Figure 4E**).

In a next step, we performed transcriptome profiling following PHF6 knockdown and confirmed significant overlapping gene signatures using 'Gene set enrichment analysis' (GSEA) between all four neuroblastoma cell lines (**Figure S3**). Overlap between the significantly differentially expressed genes (DEG) (adjusted P-value < 0.05) reveals upregulation of 730 genes while 717 genes were downregulated in at least two of the four cell lines (**Figure 5A**). The 730 common upregulated included amongst others *GATA2*, *GATA3* and *HAND2*. Interestingly, along with PHOX2B, ASCL1, TBX2, ISL1 and others, these are members of the

previously described adrenergic neuroblastoma 'core regulatory circuitry' (CRC)[43–45]. Neuroblastoma tumors are highly heterogeneous, and comprise both adrenergic and neural crest like (mesenchymal) cell types. Both cell identities are charactized by super-enhancer marked transcription factors, which are controlling the gene expression program of the two neuroblastoma cell identities[45]. In contract, genes involved in replication and replication stress response pathways comprising *FANCD2*, *CDC25A*, *CHEK1* and *AURKA* are downregulated (**Figure 5B).** Moreover, GSEA also showed upregulation of p53 pathway gene sets (**Figure 5C**), in keeping with the data of Warmerdam and colleagues, who also showed involvement of PHF6 in DNA damage induced p53 activation[9]. In addition, we observe significant downregulation of E2F and MYC target genes upon PHF6 knockdown as well as downregulation of G2/M cell cycle genes. Interestingly, gene sets related to E2F targets and MYC targets were also downregulated in our previously published RNA-seq data using siRNAs to downregulate *RRM2* expression[26]. Moreover, we also observe significant overlap in transcriptional effects after knockdown of PHF6 and RRM2 using siRNAs as well as pharmacological RRM2 inhibition using triapine (3AP), again underpinning the possible functional link between the two proteins (**Figure 5D**). Enrichment analysis using ENRICHR[29] and ConsensusPathDB[30] tools for the 717 common down regulated genes shows enrichment for genes involved in G2/M transition, as well as enrichment for genes involved in ATR signaling pathway, DNA damage response and cell cycle regulation (**Figure 5E**). We also found a significant overlap with ChIP-seq identified targets of E2F1, FOXM1 and different adrenergic CRC transcription factors, including ISL1, PHOX2B, GATA3, HAND2, MYCN and TBX2 (**Figure 5F, left**). Remarkably, also overlap with H3K9ac and H3K56ac ChIP-seq identified targets was observed (**Figure 5F, right**), both previously identified as DNA-damage responsive histone modifications[46]. Interestingly, H3K9ac has been implicated in regulating transcriptional repression after DNA damage, mediated by CHK1[47], while H3K56ac is a histone modification present in newly synthesized histones that are assembled into nascent chromatin after DNA replication and repair on the one hand but also implicated in promoter chromatin disassembly and transcriptional activation on the other hand[48,49]. Based on these observations, we confirmed binding of PHF6 to H3K56ac, which slightly increases upon low-dose etoposide treatment (0.1µM) in IMR-32 cells (**Figure 5G**), in keeping with our proposed role for PHF6 in DNA replication and repair. Acetylation of H3K56 results from CBP/EP300 activity predominantly at highly transcribed regions[50]. Interestingly, EP300 ChIP-seq targets were also enriched amongst the downregulated genes upon PHF6 knockdown (**Figure 5F, left**).

CUT&RUN reveals binding of PHF6 to the adrenergic CRC in neuroblastoma

Since H3K56ac was also shown to be a critical factor required for cell cycle re-entry after DNA repair, preferentially in rapidly turned-over nucleosomes[51], we speculate that PHF6 facilitates and controls high transcriptional rates of super-enhancer associated genes in cancer cells and that PHF6 chromatin binding, with association to H3K56ac, is required to ensure the finalization of DNA repair and subsequent release from checkpoint inhibition during replicative stress responses. Therefor, we mapped the PHF6 genome-wide binding sites using CUT&RUN analysis to in IMR-32, CLB-GA and SK-N-BE(2)-C neuroblastoma cells. Strong overlap between the binding sites of the three cell lines was observed (**Figure S4A**), resulting in 3171 genes that are bound by PHF6 in all three cell lines (**Figure S4B, left**). We subjected these genes to enrichment analysis using ENRICHR[29] and observed significant overlap with the bindings sites of FOXM1 and adrenergic CRC members PHOX1B, ISL1, MYCN, GATA3, TBX2, amongst others (**Figure S4B, right**). Peak annotation distribution analysis shows that PHF6

mainly binds to intron and intergenic regions (**Figure S4C, left**), which are significantly overlapping with active promotor/enhancer histone marks (**Figure 6A and S4C, right**). Previously, we performed CasID experiments in SK-N-BE(2)-C to identify upstream regulators of *RRM2* expression[26]. This revealed that PHF6 as well as NuRD and PAF1 protein complex members, both previously described as PHF6 interactors[6,7], are binding to the *RRM2* promotor (**Figure S4D, top**). Through CUT&RUN analysis, we confirmed the binding of PHF6 to the *RRM2* promotor in all three cell lines (**Figure S3D, bottom**). Motif analysis using HOMER revealed significant enrichment for CTCF and adrenergic CRC TF motifs of ASCL1, PHOX2A, ISL1, PHOX2B, HAND2, GATA3 and GATA2, in the PHF6 binding sites (**Figure 6B)**, again indicating significant overlap between PHF6 and the CRC transcription factors in neuroblastoma. Indeed, when comparing ChIP-seq data from the studies of Boeva *et al.*[43] and Durbin *et al.*[52], we observed significant overlap in the binding sites of PHF6 with HAND2, PHOX2B, GATA3, ASCL1 and MYCN, predominantly at the PHF6 enhancer associated peaks (**Figure 6C**). Moreover, we also observed strong overlap between the binding profiles of PHF6 and differentially expressed genes after siRNA mediated PHF6 knockdown (**Figure S3E**).
In view of our finding that PHF6 can also bind to the H3K56ac DNA-damage associated histone mark (**Figure 5E and 5F**), we also performed CUT&RUN to map H3K56ac sites in IMR-32 and CLB-GA neuroblastoma cells. This revealed significant overlap with PHF6 binding sites in keeping with PHF6-H3K56ac interaction (**Figure 6D**). Enrichment analysis using ENRICHR[29] on the overlapping binding sites in CLB-GA showed again significant enrichment for binding sites of the ADR CRC transcription factors (**Figure 6E)**. As these CRC members are known to be highly transcribed in neuroblastoma, these regions are inherently at higher risk to suffer from replicative stress[45]. Therefore, we propose that PHF6 is recruited to these regions and attracts RRM2 to relief transcription-associated DNA damage. Indeed, binding of PHF6 and H3K56ac was confirmed at the PHOX2B, GATA3, HAND2 and MYCN loci (**Figure 6F**).

Discussion

Rapidly dividing cancer cells experience high levels of replication stress due to aberrant DNA replication signaling or DNA damage insults that may result in stalling or even collapse of replication forks that eventually fuel genomic instability[4]. Data indicate that, unlike adult cancers, pediatric tumors display a paucity of mutations that affect components of the DNA damage repair (DDR) pathway[53]. Nevertheless, other genetic alterations in pediatric cancer arise that can result in synthetic lethality with the DNA damage response axis, making it an interesting therapeutic entry point also in this context. There is increasing evidence that chromatin dynamics regulate genomic stability and thus display an intricate crosstalk with the DNA damage response [5]. In that respect, recent studies have revealed that PHF6 is a key novel regulator of genomic stability, replication fork progression and DNA damage repair[8]. Beside that, the PHF6 protein has been previously identified as key ATM and ATR substrate[54] and more recently as modulator of R-loops[55], the latter being recognized as a potent source of replication stress[56]. In this study, we aimed to further elucidate the underlying mechanistic basis for the role of PHF6 in these processes.
Through immunoprecipitation-coupled mass spectrometry (IP-MS) analysis with PHF6 as bait we collected converging data towards RRM2 as a robust PHF6 interactor. Notably, studies from our lab and others have recently identified RRM2 as a critical factor in both pediatric and adult malignancies, through control of dNTP production, in regulation of replication fork

progression and as rheostat for CHK1 activation upon replication stress and DNA damage insults[26,57–61]. Through NanoBRET™-based deletion mapping, we could pinpoint the first PHD domain of PHF6 as critical interface for the physical interaction with RRM2. Protein-protein interactions are increasingly recognized as an emerging drug modality and therefore we propose that pharmacological targeting PHF6-RRM2 is a promising therapeutic approach in cancer[62]. Given that we previously identified RRM2 as key replicative stress resistor in the context of neuroblastoma[26], we aimed in this study to functionally evaluate the role of PHF6 in this tumor entity. Through CUT&RUN analyses we could show for the first time that genome-wide binding sites of PHF6 significantly overlap with those for previously described neuroblastoma specific adrenergic core regulatory circuitry (CRC) factors including MYCN, HAND2, PHOX2B, GATA3 and ISL1. In addition, these binding sites were strongly enriched at H3K4me1/H3K27ac marked active enhancers. Moreover, we also identified strong overlap with sites marked by H3K56ac, a histone modification that has been previously functionally linked to genomic stability, DNA damage signaling and most notably, enriched at sites of replication fork restart, forming so-called 'H3K56ac scars'[49,50,63]. In line with these findings, we could show that PHF6 acts as transcriptional regulator of cell cycle and DNA damage response signaling and is a putative novel biomarker for sensitivity to pharmacological CHK1 inhibition. Our IP-MS experiments also displayed enrichment for other factors in these processes. Amongst others we found a consistent enrichment for the chromatin interacting protein and DNA damage responsive factor PATZ1. Although its functional role in pediatric cancer remains enigmatic thus far, PATZ1 has been shown to be overexpressed as fusion transcript with EWSR1 in glioma[64], while a genome-scale CRISPR-cas9 screen in *MYCN* amplified neuroblastoma cells revealed dependency of neuroblastoma on PATZ1 expression as well[52]. Other recurrent PHF6 interacting hits in our IP-MS experiments included TOP2B, a factor that is recruited to stalled forks[65], ABCF1, described as sensor of genomic integrity[66] and two components of the nuclear pore complex (NPC): RANBP2, a SUMO E3 ligase and ELYS, an important factor for assembly of the NPC. Interestingly, they also functionally connect to replicative stress resistance[67–69]. The NPC is a very dynamic structure: in addition to its role as gateway between the nucleoplasm and cytoplasm, it actively participates in regulating replication fork dynamics, protection to replicative stress and DNA repair[70,71].
Altogether, our observations converge towards a role for PHF6 in control of genomic integrity and lineage identity in neuroblastoma and key adaptor protein in functional concertation with RRM2 under replicative stress.

Materials and methods

Cell culture

The human neuroblastoma cell lines (CLB-GA, IMR-32, SH-SY5Y and SK-N-BE(2)-C), the retinal pigmented epithelial cell line (RPE) and human fetal kidney–derived cell line (HEK293T) were grown in RPMI 1640 supplemented with 10% fetal calf serum (FCS), penicillin/ streptomycin (100 IU/ml), and 2 mM L-glutamine. The leukemia cell line ALL-SIL was grown in RPMI 1640 supplemented with 20% fetal calf serum (FCS), penicillin/ streptomycin (100 IU/ml), and 2 mM L-glutamine. HCT116 cells were cultured in McCoy's 5A medium also supplemented with 10% fetal calf serum (FCS), penicillin/ streptomycin (100 IU/ml), and 2 mM L-glutamine. All cell lines used were cultured in 5% CO2 atmosphere at 37°C on plastic cultured plates. Short Tandem Repeat (STR) genotyping was used to validate cell line authenticity prior to performing the

described experiments and Mycoplasma testing was done on a monthly basis. Origin of products used for cell culture can be found in **Table S3**.

Co-immunoprecipitation followed by mass-spectrometry or Western Blot analysis

Co-immunoprecipitation (co-IP) with PHF6 as bait protein was performed by lysing 10M cells/sample in 1ml cold radioimmunoprecipitation assay (RIPA) buffer (12.7 mM; 150 mM NaCl, 50 mM Tris-HCl (pH 7.5), 0.01% SDS solution, and 0.1% NP-40) supplemented with protease and phosphatase inhibitors. Lysates were incubated with 2µg antibody (PHF6 or human IgG) for 4 hours. After adding 20 µl Protein A UltraLink® Resin (Life Technologies, 53139), the mixture was rotated overnight at 4°C.

For the IP-MS analysis, after the overnight incubation, Peptides were re-dissolved in 20 µl loading solvent A (0.1% TFA in water/ACN (98:2, v/v)) of which 2 µl was injected for LC-MS/MS analysis on an Ultimate 3000 RSLC nano LC (Thermo Fisher Scientific, Bremen, Germany) in-line connected to a Q Exactive mass spectrometer (Thermo Fisher Scientific). Trapping was performed at 10 µl/min for 4 min in loading solvent A on a 20 mm trapping column (made in-house, 100 µm internal diameter (I.D.), 5 µm beads, C18 Reprosil-HD, Dr. Maisch, Germany). The peptides were separated on a 25 cm in needle packed column (made in-house, 75 µm internal diameter (I.D.), 3 µm beads, C18 Reprosil-HD, Dr. Maisch, Germany) kept at a constant temperature of 50°C). For ALL-SIL, CLB-GA and IMR-32, peptides were eluted by a non-linear gradient starting at 2% MS solvent B reaching 55% MS solvent B (0.1% FA in water/acetonitrile (2:8, v/v)) in 123 min, 99% MS solvent B in 12 minutes followed by a 6-minute wash at 70% MS solvent B and re-equilibration with MS solvent A (0.1% FA in water). For the other cell lines, peptides were eluted by a linear gradient reaching 30% MS solvent B (0.1% FA in water/acetonitrile (2:8, v/v)) after 74 (SK-N-BE(2)-C, SH-SY5Y and HCT116)/ 104 (HEK293T and RPE, 50% MS solvent B after 99 min (SK-N-BE(2)-C, SH-SY5Y and HCT116) / 121 min (HEK293T and RPE) and 99% MS solvent B at 100 min (SK-N-BE(2)-C, SH-SY5Y and HCT116) / 125 min (HEK293T and RPE) , followed by a 5-minutes wash at 99% (SK-N-BE(2)-C, SH-SY5Y and HCT116) / 70% (HEK293T and RPE) MS solvent B and re-equilibration with MS solvent A (0.1% FA in water). The first 9 min the flow rate was set to 750 nl/min after which it was kept constant at 300 nl/min. The mass spectrometer was operated in data-dependent mode, automatically switching between MS and MS/MS acquisition for the 5 (IMR-32) / 10 (other cell lines) most abundant ion peaks per MS spectrum. Full-scan MS spectra (400-2000 m/z) were acquired at a resolution of 70,000 in the Orbitrap analyzer after accumulation to a target value of 3,000,000. The 5 (IMR-32) / 10 (other cell lines) most intense ions above a threshold value of 13,000 (IMR-32) / 17,000 (other cell lines) were isolated with a width of 2 m/z for fragmentation at a normalized collision energy of 25% after filling the trap at a target value of 50,000 for maximum 80 (IMR-32) / 60 (other cell lines). MS/MS spectra (200-2000 m/z) were acquired at a resolution of 17,500 in the Orbitrap analyzer.

Analysis of the mass spectrometry data was performed in MaxQuant (version 2.2.0.0) with mainly default search settings including a false discovery rate set at 1% on PSM, peptide and protein level. Spectra were searched against the human reference proteome (version of 01_2023, UP000005640). The mass tolerance for precursor and fragment ions was set to 4.5 and 20 ppm, respectively, during the main search. Enzyme specificity was set as C-terminal to arginine and lysine, also allowing cleavage at proline bonds with a maximum of two missed cleavages. Variable modifications were set to oxidation of methionine residues and acetylation of protein N-termini. Matching between runs was enabled with a matching time window of 0.7 minutes and an alignment time window of 20 minutes. Only proteins with at

least one unique or razor peptide were retained. Proteins were quantified by the MaxLFQ algorithm integrated in the MaxQuant software. A minimum ratio count of two unique or razor peptides was required for quantification. Further data analysis of the results was performed with an in-house R script, using the proteinGroups output table from MaxQuant. Reverse database hits were removed, LFQ intensities were log2 transformed and replicate samples were grouped. Proteins with less than three valid values in at least one group were removed and missing values were imputed from a normal distribution centered around the detection limit (package DEP[72]). To compare protein abundance between pairs of sample groups (IgG vs PHF6 sample groups), statistical testing for differences between two group means was performed, using the package limma[73]. Statistical significance for differential regulation was set to a false discovery rate (FDR) of <0.05 and $|\log2FC| \geq 0.6$.
For the co-IP based validation of the PHF6-RRM2 interaction through immunoblotting, the mixtures were centrifugated, after overnight incubation on 4°C, for 2min at 2000 rpm and washed in RIPA buffer three times. The samples were denaturated in 1X Laemli denaturation buffer supplemented with β-mercaptoethanol and incubated at 95°C for 10minutes. The denatured samples were loaded on 10% SDS–polyacrylamide gel electrophoresis (SDS- PAGE) gels with 10× Tris/Glycine/SDS buffer and run for 1 hour at 100 V, blotted on nitrocellulose membranes in 10% of 10× Tris/Glycine buffer for 1 hour at 100 V. The membranes were blocked during 1 hour in 5% milk in Tris-buffered saline with 0.1% Tween® 20 detergent (TBST). Primary antibody incubations with the RRM2, H3K56ac or PHF6 antibody (Table S2) were done in blocking buffer overnight at 4°C. Blots were washed three times with TBST before the incubation for 1 hour with Veriblot secondary antibodies. The immunoblots were visualized by the enhanced chemiluminescent West Dura or West Femto (Bio-Rad). Origin of products used for Western Blotting can be found in **Table S3,** antibodies used can be found in **Table S2.**

NanoBRET™ analysis

The NanoBRET™ Nano-Glo detection System (Promega) was used according to the manufacturer's instructions. In short, expression plasmids with RRM2 or PHF6 fused to HaloTag® or NanoLuc® at N or C terminal site, were made using the NanoBRET™ PPI MCS Starter System (Promega, cat n° N1811). The RRM2 fragments were amplified by PCR using Phusion polymerase (NEB, M0530L) and OriGene clone GC-Z9335-GS as template. For PHF6 fragments, OriGene clone GC-Z2633-CF served as template. All fragments and vectors pNLF1-C (CMV/Hygro), pNLF1-N (CMV/Hygro), pHTN HaloTag® CMV-neo and pHTC HaloTag® CMV-neo were digested with restriction enzymes and subsequently ligated (Takara, cat n°6023). Primers and corresponding restriction digests can be found in the **Table S5**. The sequences of the constructed plasmids were verified by Sanger DNA sequencing (Eurofins Genomics, SupremeRun Tube Service) and the overexpression in HEK293T was validated using a Simple Western™ automated blot system (WES™ system, ProteinSimple, Bio-Techne) according to manufacturer's instructions. In total, 1.2 µg of protein lysate was used, primary antibodies anti-PHF6, anti-RRM2 and anti-NanoLuc® antibody were used (see **Table S2** for antibody information). Next, HEK293T cells were co-transfected with HaloTag and Nluc fusions using FuGENE reagent (Promega). After 20h, the transfected cells were trypsinized, washed with PBS, resuspended in assay medium (Opti-MEM I Reduced Serum Medium, no phenol red, supplemented with 4% FBS), re-plated to a 96-well plate, and incubated overnight with HaloTag NanoBRET™ 618 Ligand (100 nmol/L final concentration) or DMSO as negative control. NanoBRET™ Nano-Glo Substrate was added, donor emission (460 nm) and acceptor emission (618 nm) signals were measured using the GloMax Discover System (Promega). Raw

NanoBRET™ ratio values with milliBRET units (mBU) were calculated as RawBRET = (618 nm Em/460 nm Em) × 1000. Corrected NanoBRET™ ratio values with milliBRET units were calculated as corrected BRET = RawBRET of experimental sample – RawBRET of negative control sample, which reflected energy transfer from the bioluminescent protein donor to the fluorescent protein acceptor reflecting the protein-protein interaction.

siRNA-mediated knockdown of PHF6

IMR-32, CLB-GA, SH-SY5Y and SK-N-BE(2)-C neuroblastoma cells were transfected using the Neon transfection system (MPK10096) with two siRNAs toward PHF6: siPHF6-48 (s38848, Life technologies, #439242) and siPHF6-SP (SMARTPool 84295, Dharmacon, L-014862-00-0005). As negative control, a scrambled siRNA (Ambion, #AM4635) was used. After transfection, cells were seeded in a T-25 flask at a density of 2 x 10^6 cells per flask. For proliferation analysis, 2000 to 3000 cells/well were seeded in a 384-well plate and analyzed using the IncuCyte™ Live Cell Imaging System. Each image was analyzed through the IncuCyte Software and cell proliferation was determined by the area (percentage of confluence) of cell images over time. The cells seeded in a T-25 flask were collected for RNA and protein isolation, 48 hours after transfection. Knockdown of PHF6 was evaluated by RT-qPCR and immunoblotting.

Western Blotting

Cells were lysed in RIPA supplemented with protease and phosphatase inhibitors and rotated for 1 hour at 4°C. The lysates were cleared by centrifugation at 10,000 rpm in a microcentrifuge for 10 min at 4°C. Concentrations were determined using the Pierce BCA Protein Assay Kit. The lysates were denaturized before loading on a gel, by adding 5X Laemli denaturation buffer supplemented with β–mercaptoethanol. 30µg of protein extracts were loaded on SDS-PAGE gels with 10× Tris/Glycine/SDS buffer and run for 1 hour at 100 V. Samples were blotted on nitrocellulose or polyvinylidene difluoride (PVDF) membranes in 1x Tris/Glycine buffer and 20% of methanol. The membranes were blocked during 1 hour in 5% nonfat dry milk or 5% BSA in TBST. Primary antibody incubations for PHF6, pCHK1(Ser345), CHK1, pRPA32, RPA32, γH2AX, β-actin and vinculin were done in blocking buffer overnight at 4°C. Blots were washed three times with TBST and incubated for 1 hour with secondary antibodies. The immunoblots were visualized by using the enhanced chemiluminescent WES Dura or WES Femto (Bio-Rad). Quantification was performed through ImageJ software, where the area from each protein was normalized to the loading protein in respect to each blot. Products used for Western Blotting can be found in **Table S3**, antibodies can be found in **Table S2.**

RNAseq and RT-qPCR validation

RNA was isolated using the miRNeasy kit from QIAGEN including an on-column deoxyribonuclease treatment. Concentrations were measured using NanoDrop (Thermo Fisher Scientific). Libraries for mRNA-seq were prepared using the QuantSeq 3' mRNA library prep kit (Lexogen, Vienna, Austria) with UMI barcoding according to the manufacturer's protocol. The libraries were equimolarly pooled and sequenced on an Illumina NextSeq 500 high-throughput flow cell, generating single-end 75-bp reads. Adequate sequencing quality was confirmed using FastQC version 0.11.8 (Andrews, 2010). To remove the "QuantSEQ FWD" adaptor sequence, the reads were trimmed using cutadapt version 1.18. The trimmed reads were mapped to the human reference genome (GRCh38.89) using the STAR aligning software v 2.6.0c. The RSEM software, version v1.3.1, was used to generate count tables. Genes were

only retained if they were expressed at counts per million (cpm) above one in at least three samples. Counts were normalized with using the TMM method (R-package edgeR, v3.36.0), followed by Voom transformation and differential expression analysis using Limma (R-package limma, v3.503.3). Principal component analysis showed that sample "CLBGA siPHF6a replicate 3" is an outlier so this sample was removed from further analysis. A general linear model was built with the treatment groups and the replicates as a batch effect. Gene Set Enrichment Analysis (GSEA) was performed on the genes ordered according to differential expression statistic value (t). Signature scores were conducted using a rank-scoring algorithm. GSEA was done using the Hallmark gene set collection from MSigDB (gsea-msigdb.org) or gene lists compiled from this or our previous study (GSE161902). All RNA-seq data are available through the Gene Expression Omnibus (GEO) repository (GSE226288).
For RT-qPCR, complementary DNA (cDNA) synthesis was done using the iScript Advanced cDNA synthesis kit from Bio-Rad. The PCR mix was composed out of 5 ng of cDNA, 2.5 µl of SsoAdvanced SYBR qPCR super mix (Bio-Rad), and 0.25 µl of forward and reverse primers (to a final concentration of 250 nM; Integrated DNA Technologies). The RT- qPCR cycling analysis was performed using a LC-480 device (Roche). qBasePlus software 3.2 (www.biogazelle.com) was used for the analysis of the gene expression levels. B2M, HPRT1, TBP, and HMBS were used as reference genes. The error bars in figures represent SD after error propagation, with mean centering and scaling to control. The primer designs are provided in **Table S1**.

CUT&RUN

CUT&RUN coupled with high-throughput DNA sequencing was performed on isolated nuclei using Cutana pA/G-MNase (Epicypher, 15-1016) according to the manufacturer's manual. Briefly, nuclei were isolated from 0.5M cells/sample in 100µl nuclear extraction buffer per sample and incubated with activated Concanavalin A beads for 10 min at 4°C while rotating. Nuclei were resuspended in 50µl antibody buffer containing a 1:100 dilution of each antibody (see **Table S2** for antibody information) and kept in an elevated angle on a nutator at 4°C overnight. Next, targeted digestion and release was performed with 2.5 µL Cutana pA/G-MNase (15-1116) and 100mM $CaCl_2$ for 2 hours at 4°C on the nutator. After chromatin release by incubation on 37°C for 10 minutes, DNA was purified using the CUTANA DNA purification kit (14-0050) and eluted in 12µl of elution buffer. Sequencing libraries were prepared with the NEBNext Ultra II kit (Illumina, E7645), followed by paired-end sequencing on a Nextseq2000 using the NextSeq 2000 P2 Reagents 100 Cycles v3 (Illumina, 20046811). Prior to mapping to the human reference genome (GRCh37/hg19) with bowtie2 (v.2.3.1), quality of the raw sequencing data of CUT&RUN was evaluated using FastQC and adapter trimming was done using TrimGalore (v0.6.5). Quality of aligned reads were filtered using min MAPQ 30 and reads with known low sequencing confidence were removed using Encode Blacklist regions. For sample with a percentage duplicated reads higher then 10%, deduplication was performed using MarkDuplicates (Picard, v4.0.11). Peak calling was performed using MACS2 (v2.1.0) taking a q value of 0.05 as threshold and default parameters. Homer (v4.10.3) was used to perform motif enrichment analysis, with 200 bp around the peak summit as input. Overlap of peaks, annotation, heatmaps and pathway enrichment was analysed using DeepTools (v3.5.1), the R package ChIPpeakAnno (v3.28.1), and the web tool ENRICHR. The R package igvR (v1.19.3) was used for visualization of the data upon RPKM normalization. All CUT&RUN data are available through the Gene Expression Omnibus (GEO) repository (GSE226288).

Acknowledgements

We would like to thank prof. dr. Frank Speleman for the guidance and support in the experimental design and conceptualization of this manuscript; and prof. dr. Francis Impens and Sara Dufour for the technical assistance and subsequent data-analysis of the IP-MS experiments. This research was supported by the following funding agencies: Olivia Fund, 'Kinderkankerfonds', Ghent University (BOF.GOA.2022.0003.03 and BOF.STG.2022.0009.01) and Fund for Scientific Research Flanders (project G037918N).

Figure legends

Figure 1. **PHF6 interacts with RRM2 and proteins involved in nuclear transport, SUMOylation and cell cycle regulation. (A)** Volcano plot displaying significantly enriched putative PHF6 interactors by means of immunoprecipitation-coupled mass spectrometry (IP-MS) in HEK293T cells; **(B)** Venn diagram showing PHF6 interactors commonly identified between IP-MS experiments in HEK293T and CLB-GA, IMR-32, SK-N-BE(2)-C and SH-SY5Y neuroblastoma cell lines; **(C)** ENRICHR and **(D)** ConsensusPathDB over-representation analysis showing functional enrichment of PHF6 interacting proteins in processes such as cell cycle regulation, gene expression, rRNA processing, SUMOylation, nuclear transport and replication.

Figure 2. **PHF6 interacts with RRM2 through its first PHD domain. (A)** Immunoblotting for RRM2 (*right*) and PHF6 (*left*) following co-immunoprecipitation analysis using PHF6 as bait in HEK293T (*top*) and IMR-32 (*bottom*) cells. **(B)** Schematic overview of the NanoBRET™ assay for detecting protein-protein interactions by measuring the energy transfer between a NanoLuc® luciferase (Nluc) donor fusion protein with PHF6 and a HaloTag® (HT) acceptor fusion protein with RRM2. Energy transfer only occurs when the fusion proteins are in close proximity to one another (<10nm); **(C)** Mean corrected NanoBRET™ ratios resulting from different amounts of transfected Nluc-PHF6 and RRM2-HT encoding constructs in HEK293T cells; **(D)** Donor saturation assay for the Nluc-PHF6 + RRM2-HT combination results in hyperbolic increase in NanoBRET™ signal; **(E)** (*left*) Mean corrected NanoBRET™ ratios from transfecting 11 different deletion constructs of PHF6 fused to Nluc (Fr1-Fr11) together with the RRM2-HT fusion. Error bars represent the mean ± SEM of 2 to 4 biological replicates (represented by dots) and (*right*) schematic representation of the deletion constructs, sorted from highest to lowest mean NanoBRET™ ratio; **(F)** HEK293T cells were transfected with 2µg RRM2-HT, 0.2µg Nluc-PHF6 and 0.2µg of the deletion constructs Fr1-F11 fused to Nluc. Protein expression levels were analyzed with Simple WES using anti-RRM2, anti-PHF6 and anti-Nluc antibodies respectively.

Figure 3. **High *PHF6* expression is correlated with poor prognosis in primary neuroblastoma. (A)** Log_2 expression of *PHF6* mRNA throughout different cancer cell lines from the 'Cancer Cell Line Encyclopedia' (CCLE) database. The boxplots represent the 1st to 3rd quartile of the data values, with the line representing the median value. Whiskers represent values of the outer two quartiles maximized at 1.5 times the size of the box ('x' indicates one or more values outside of the whiskers); **(B)** *Phf6* mRNA expression is up-regulated during TH-MYCN–driven neuroblastoma tumor development[74] ($p = 2.43 \times 10^{-6}$); **(C)** High *PHF6* expression levels correlate to poor event-free ($p = 3.5 \times 10^{-5}$) and overall ($p = 1.5 \times 10^{-7}$) neuroblastoma patient survival [Kocak cohort (n = 283); hgserver2.amc.nl]; **(D)** *PHF6* expression is higher in Stage 4 neuroblastoma patients compared to other risk groups (left, $p < 0.001$) and in *MYCN*-amplified

neuroblastomas compared to *MYCN* non amplified cases (right, $p = 2.7 \times 10^{-20}$) [Kocak cohort (n = 283); hgserver2.amc.nl].

Figure 4. **High *PHF6* expression as putative biomarker for pharmacological CHK1 inhibitor sensitivity. (A)** *PHF6* mRNA expression levels and **(B)** PHF6 protein expression levels upon siRNA mediated PHF6 knockdown in IMR-32, CLB-GA, SK-N-BE(2)-C and SH-SY5Y neuroblastoma cell lines using two different siRNAs (siPHF6_48 and siPHF6_SP) and one no template control siRNA (siNTC). Error bars represent the mean ± SEM of 4 biological replicates (represented by dots); **(C)** IncuCyte™ live cell imaging analysis upon transfection of IMR-32 cells with siPHF6_48 and siPHF6_SP. Non transfected IMR-32 cells and cells transfected with siNTC were used as controls; **(D)** (*left*) Immunoblotting for various DNA damage markers in IMR-32 cells upon siRNA mediated knockdown of PHF6, (*right*) Quantification of the blot using ImageJ is shown; **(E)** Signature score analysis of prexasertib sensitivity and resistance gene signatures in a large primary cohort of neuroblastoma cases (GSE62564).

Figure 5. PHF6 knockdown leads to downregulation of neuroblastoma ADR CRC regulated and H3K56ac associated gene signatures. (A) Venn diagram showing the overlap of up- and downregulated genes identified by RNA-sequencing upon PHF6 knockdown in CLB-GA, SK-N-BE(2)-C, SH-SY5Y and IMR-32 neuroblastoma cells compared to the siRNA control; **(B)** Volcano plot displaying significantly upregulated (red) and downregulated (blue) genes upon siRNA mediated knockdown of PHF6 in CLB-GA cells; **(C)** Gene set enrichment analysis (GSEA) of the RNA-seq based transcriptome profiles after PHF6 knockdown in CLB-GA cells using the Hallmark MSigDB gene sets; **(D)** GSEA shows a significant overlap between up- and down regulated genes upon PHF6 knockdown using siRNAs and genes downregulated following either RRM2 knockdown pharmacological RRM2 inhibition using 3AP (GSE161902); **(E)** ConsensusPathDB over-representation analysis of downregulated genes upon PHF6 knockdown showing enrichment in amongst others DNA damage response and cell cycle checkpoint regulation processes; **(F)** Enrichment analysis using ENRICHR of the downregulated genes upon PHF6 knockdown shows enrichment for ChIP-sequencing identified targets of E2F1, FOXM1 and neuroblastoma adrenergic core regulatory circuitry members (ADR CRC) including ISL1, PHOX2B, GATA3, HAND2, MYCN and TBX2 (*left*) as well as H3K27ac, H3K4me3, H3K9ac and H3K56ac associated genes amongst others (*right*); **(G)** Immunoblotting for PHF6 (top) and H3K56ac (bottom) after co-immunoprecipitation analysis with H3K56ac as using two different antibodies (ab1 and ab2) in IMR-32 neuroblastoma cells upon DMSO and etoposide treatment (0.1µM).

Figure 6. CUT&RUN reveals binding of PHF6 to the ADR CRC in neuroblastoma. (A) Heatmap profiles −4kb and +4kb around the summit of PHF6 CUT&RUN peaks, representing overlap of PHF6 with CUT&RUN peaks of H3K4me3, H3K27ac, H3K4me3 and H3K4me1 in IMR-32 neuroblastoma cells, grouped for promoters or enhancers (using homer annotation), and ranked according to the sums of the peak scores across all datasets in the heatmap; **(B)** Homer motif analysis of the PHF6 CUT&RUN peaks in IMR-32 cells; **(C)** Heatmap profiles −2kb and +2kb around the summit of PHF6 CUT&RUN peaks, representing overlap of PHF6 CUT&RUN peaks in IMR-32 cells with MYCN CUT&RUN peaks as well as publicly available ChIP-seq peaks of HAND2, PHOX2B and GATA3 in CLB-GA [GSE90683], ASCL1 in SK-N-BE(2)-C [GSE159613] which were grouped for promoters or enhancers (using homer annotation), and ranked according to the sums of the peak scores across all datasets in the heatmap; **(D)** Venn diagram

(*top*) and heatmap profiles −4kb and +4kb around the summit of PHF6 CUT&RUN peaks (*bottom)* showing the significant overlap (min overlap = 10 bp) between PHF6 and H3K56ac CUT&RUN peaks in IMR-32 (Fisher's Exact Test p-value < 2.2×10^{-16}) and CLB-GA cells (Fisher's Exact Test p-value < 2.2×10^{-16}). For the heatmap, peaks were ranked according to the sums of the peak scores across the datasets in the heatmap; **(E)** Enrichment analysis using ENRICHR of the PHF6 and H3K56ac overlapping peaks in CLB-GA shows enrichment for ChIP-seq identified targets of CTCF, FOXM1 and ADR CRC members ISL1, PHOX2B, HAND2, TBX2, GATA3 and MYCN; **(F)** PHF6 and H3K56ac binding activity at the PHOX2B, GATA3, HAND2 and MYCN loci in IMR-32 cells. Signals represent log likelihood ratio for the CUT&RUN signal compared to control signal (RPKM normalized). All peaks are called by MACS2 (q<0.05).

References

1. Hanahan, D. & Weinberg, R. A. *Hallmarks of cancer: The next generation*. *Cell* vol. 144 646–674 (Cell Press, 2011).
2. Ngoi, N. Y. L., Pham, M. M., Tan, D. S. P. & Yap, T. A. Targeting the replication stress response through synthetic lethal strategies in cancer medicine. *Trends in Cancer* **7**, 930–957 (2021).
3. Nickoloff, J. A. Targeting Replication Stress Response Pathways to Enhance Genotoxic Chemo- and Radiotherapy. *Molecules (Basel, Switzerland)* vol. 27 4736 (2022).
4. Kotsantis, P., Petermann, E. & Boulton, S. J. Mechanisms of oncogene-induced replication stress: Jigsaw falling into place. *Cancer Discovery* vol. 8 537–555 (2018).
5. Rother, M. B. & van Attikum, H. DNA repair goes hip-hop: SMARCA and CHD chromatin remodellers join the break dance. *Philos. Trans. R. Soc. B Biol. Sci.* **372**, (2017).
6. Todd, M. A. M. & Picketts, D. J. PHF6 interacts with the nucleosome remodeling and deacetylation (NuRD) complex. *J. Proteome Res.* **11**, 4326–4337 (2012).
7. Zhang, C. *et al.* The X-Linked Intellectual Disability Protein PHF6 Associates with the PAF1 Complex and Regulates Neuronal Migration in the Mammalian Brain. *Neuron* **78**, 986–993 (2013).
8. Alvarez, S. *et al.* Functional mapping of PHF6 complexes in chromatin remodeling, replication dynamics, and DNA repair. *Blood* **139**, 3418–3429 (2022).
9. Warmerdam, D. O. *et al.* PHF6 promotes non-homologous end joining and G2 checkpoint recovery. *EMBO Rep.* (2019) doi:10.15252/embr.201948460.
10. Aasland, R., Gibson, T. J. & Stewart, A. F. The PHD finger: Implications for chromatin-mediated transcriptional regulation. *Trends Biochem. Sci.* **20**, 56–59 (1995).
11. Mellor, J. It Takes a PHD to Read the Histone Code. *Cell* **126**, 22–24 (2006).
12. Chao, M. M. *et al.* T-cell acute lymphoblastic leukemia in association with Börjeson-Forssman-Lehmann syndrome due to a mutation in PHF6. *Pediatr. Blood Cancer* **55**, 722–724 (2010).
13. Lower, K. M. *et al.* Mutations in PHF6 are associated with Börjeson-Forssman-Lehmann syndrome. *Nat. Genet.* **32**, 661–665 (2002).
14. Wieczorek, D. *et al.* A comprehensive molecular study on Coffin-Siris and Nicolaides-Baraitser syndromes identifies a broad molecular and clinical spectrum converging on altered chromatin remodeling. *Hum. Mol. Genet.* **22**, 5121–5135 (2013).
15. Voss, A. K. *et al.* Protein and gene expression analysis of Phf6, the gene mutated in the Börjeson–Forssman–Lehmann Syndrome of intellectual disability and obesity. *Gene Expr. Patterns* **7**, 858–871 (2007).
16. Van Vlierberghe, P. *et al.* PHF6 mutations in T-cell acute lymphoblastic leukemia. *Nat. Genet.* **42**, 338–342 (2010).
17. Van Vlierberghe, P. *et al.* PHF6 mutations in adult acute myeloid leukemia. *Leuk. 2011 251* **25**, 130–134 (2010).
18. Li, X. *et al.* Somatic mutations of PHF6 in patients with chronic myeloid leukemia in blast crisis. *Leukemia and Lymphoma* vol. 54 671–672 (2013).
19. Xiao, W. *et al.* PHF6 and DNMT3A mutations are enriched in distinct subgroups of mixed phenotype acute leukemia with T-lineage differentiation. *Blood Adv.* **2**, 3526–3539 (2018).
20. Yoo, N. J., Kim, Y. R. & Lee, S. H. Somatic mutation of PHF6 gene in T-cell acute lymphoblatic leukemia, acute myelogenous leukemia and hepatocellular carcinoma. *Acta Oncol. (Madr).* **51**, 107–111 (2012).
21. Huether, R. *et al.* The landscape of somatic mutations in epigenetic regulators across 1,000 paediatric cancer

genomes. *Nat. Commun.* **5**, 1–7 (2014).
22. Hajjari, M., Salavaty, A., Crea, F. & Kee Shin, Y. The potential role of PHF6 as an oncogene: a genotranscriptomic/proteomic meta-analysis. *Tumor Biol.* **37**, 5317–5325 (2016).
23. Li, M. *et al.* Transcriptional expressions of hsa-mir-183 predicted target genes as independent indicators for prognosis in bladder urothelial carcinoma. *Aging (Albany. NY).* **14**, (2022).
24. Wang, X. *et al.* PHF6 promotes the progression of endometrial carcinoma by increasing cancer cells growth and decreasing T- - cell infiltration. 1–13 (2022) doi:10.1111/jcmm.17638.
25. Loontiens, S. *et al.* PHF6 Expression Levels Impact Human Hematopoietic Stem Cell Differentiation. *Front. Cell Dev. Biol.* **8**, (2020).
26. Nunes, C. *et al.* RRM2 enhances MYCN-driven neuroblastoma formation and acts as a synergistic target with CHK1 inhibition. *Sci. Adv.* **8**, 1382 (2022).
27. Matthay, K. K. *et al.* Neuroblastoma. *Nat. Rev. Dis. Prim.* 918–929 (2016) doi:10.4324/9781315113968.
28. Pontarin, G. *et al.* Ribonucleotide reduction is a cytosolic process in mammalian cells independently of DNA damage. *Proc. Natl. Acad. Sci. U. S. A.* **105**, 17801–17806 (2008).
29. Xie, Z. *et al.* Gene Set Knowledge Discovery with Enrichr. *Curr. Protoc.* **1**, e90 (2021).
30. Kamburov, A., Wierling, C., Lehrach, H. & Herwig, R. ConsensusPathDB—a database for integrating human functional interaction networks. *Nucleic Acids Res.* **37**, D623–D628 (2009).
31. Todd, M. A. M., Ivanochko, D. & Picketts, D. J. Phf6 degrees of separation: The multifaceted roles of a chromatin adaptor protein. *Genes (Basel).* **6**, 6 (2015).
32. Dale, N. C., Johnstone, E. K. M., White, C. W. & Pfleger, K. D. G. NanoBRET: The bright future of proximity-based assays. *Front. Bioeng. Biotechnol.* **7**, 56 (2019).
33. Liu, Z. *et al.* Structural and functional insights into the human börjeson-forssman- lehmann syndrome-associated protein PHF6. *J. Biol. Chem.* **289**, 10069–10083 (2014).
34. Murthy, S. & Reddy, G. P. V. Replitase: Complete machinery for DNA synthesis. *Journal of Cellular Physiology* vol. 209 711–717 (2006).
35. Técher, H., Koundrioukoff, S., Nicolas, A. & Debatisse, M. The impact of replication stress on replication dynamics and DNA damage in vertebrate cells. *Nat. Rev. Genet.* **18**, 535–550 (2017).
36. Weiss, W. A., Aldape, K., Mohapatra, G., Feuerstein, B. G. & Bishop, J. M. Targeted expression of MYCN causes neuroblastoma in transgenic mice. *EMBO J.* **16**, 2985–2995 (1997).
37. Decaesteker, B. *et al.* From DNA Copy Number Gains and Tumor Dependencies to Novel Therapeutic Targets for High-Risk Neuroblastoma. *J. Pers. Med. 2021, Vol. 11, Page 1286* **11**, 1286 (2021).
38. Depuydt, P. *et al.* Genomic Amplifications and Distal 6q Loss: Novel Markers for Poor Survival in High-risk Neuroblastoma Patients. *JNCI J. Natl. Cancer Inst.* **110**, 1084–1093 (2018).
39. Parsons, D. W. *et al.* Diagnostic Yield of Clinical Tumor and Germline Whole-Exome Sequencing for Children With Solid Tumors. *JAMA Oncol.* **2**, 616–624 (2016).
40. Feliciano, Y. M. S. *et al.* PHF6 regulates phenotypic plasticity through chromatin organization within lineage-specific genes. *Genes Dev.* **31**, 973–989 (2017).
41. Cole, K. A. *et al.* RNAi screen of the protein kinome identifies checkpoint kinase 1 (CHK1) as a therapeutic target in neuroblastoma. *Proc. Natl. Acad. Sci. U. S. A.* **108**, 3336–3341 (2011).
42. Blosser, W. D. *et al.* A pan-cancer transcriptome analysis identifies replication fork and innate immunity genes as modifiers of response to the CHK1 inhibitor prexasertib. *Oncotarget* **11**, 216–236 (2020).
43. Boeva, V. *et al.* Heterogeneity of neuroblastoma cell identity defined by transcriptional circuitries. *Nat. Genet.* **49**, 1408–1413 (2017).
44. Van Groningen, T. *et al.* Neuroblastoma is composed of two super-enhancer-associated differentiation states. *Nat. Genet.* **49**, 1261–1266 (2017).
45. Shendy, N. A. M., Zimmerman, M. W., Abraham, B. J. & Durbin, A. D. Intrinsic transcriptional heterogeneity in neuroblastoma guides mechanistic and therapeutic insights. *Cell Reports Medicine* vol. 3 100632 (2022).
46. Tjeertes, J. V., Miller, K. M. & Jackson, S. P. Screen for DNA-damage-responsive histone modifications identifies H3K9Ac and H3K56Ac in human cells. *EMBO J.* **28**, 1878–1889 (2009).
47. Shimada, M. *et al.* Chk1 Is a Histone H3 Threonine 11 Kinase that Regulates DNA Damage-Induced Transcriptional Repression. *Cell* **132**, 221–232 (2008).
48. Williams, S. K., Truong, D. & Tyler, J. K. Acetylation in the globular core of histone H3 on lysine-56 promotes chromatin disassembly during transcriptional activation. *Proc. Natl. Acad. Sci. U. S. A.* **105**, 9000–9005 (2008).
49. Yuan, J., Pu, M., Zhang, Z. & Lou, Z. Histone H3-K56 acetylation is important for genomic stability in mammals. *Cell Cycle* (2009) doi:10.4161/cc.8.11.8620.
50. Das, C., Lucia, M. S., Hansen, K. C. & Tyler, J. K. CBP/p300-mediated acetylation of histone H3 on lysine 56. *Nature* **459**, 113–117 (2009).

51. Masumoto, H., Hawke, D., Kobayashi, R. & Verreault, A. A role for cell-cycle-regulated histone H3 lysine 56 acetylation in the DNA damage response. *Nature* **436**, 294–298 (2005).
52. Durbin, A. D. *et al.* Selective gene dependencies in MYCN-amplified neuroblastoma include the core transcriptional regulatory circuitry. *Nat. Genet.* **50**, 1240–1246 (2018).
53. Gröbner, S. N. *et al.* The landscape of genomic alterations across childhood cancers. *Nature* **555**, 321–327 (2018).
54. Matsuoka, S. *et al.* ATM and ATR substrate analysis reveals extensive protein networks responsive to DNA damage. *Science (80-.).* **316**, 1160–1166 (2007).
55. Yan, Q. *et al.* Proximity labeling identifies a repertoire of site-specific R-loop modulators. *Nat. Commun.* **13**, 1–17 (2022).
56. Saxena, S. & Zou, L. Hallmarks of DNA replication stress. *Molecular Cell* vol. 82 2298–2314 (2022).
57. Jiang, X. *et al.* RRM2 silencing suppresses malignant phenotype and enhances radiosensitivity via activating cGAS/STING signaling pathway in lung adenocarcinoma. *Cell Biosci.* **11**, 1–20 (2021).
58. Zhuang, S., Li, L., Zang, Y., Li, G. & Wang, F. RRM2 elicits the metastatic potential of breast cancer cells by regulating cell invasion, migration and VEGF expression via the PI3K/AKT signaling. *Oncol. Lett.* **19**, 3349–3355 (2020).
59. Mazzu, Y. Z. *et al.* A Novel Mechanism Driving Poor-Prognosis Prostate Cancer: Overexpression of the DNA Repair Gene, Ribonucleotide Reductase Small Subunit M2 (RRM2). *Clin. Cancer Res.* **25**, 4480–4492 (2019).
60. Fatkhutdinov, N. *et al.* Targeting RRM2 and Mutant BRAF is a Novel Combinatorial Strategy for Melanoma. *Mol. cancer res* **14**, 767–775 (2017).
61. Ohmura, S. *et al.* Translational evidence for RRM2 as a prognostic biomarker and therapeutic target in Ewing sarcoma. *Mol. Cancer* **20**, (2021).
62. Matos, B., Howl, J., Jerónimo, C. & Fardilha, M. The disruption of protein-protein interactions as a therapeutic strategy for prostate cancer. *Pharmacol. Res.* **161**, 105145 (2020).
63. Whale, A. J., King, M., Hull, R. M., Krueger, F. & Houseley, J. Stimulation of adaptive gene amplification by origin firing under replication fork constraint. *Nucleic Acids Res.* **50**, 915–936 (2022).
64. Siegfried, A. *et al.* EWSR1-PATZ1 gene fusion may define a new glioneuronal tumor entity. *Brain Pathol.* **29**, 53–62 (2019).
65. Tian, T. *et al.* The ZATT-TOP2A-PICH Axis Drives Extensive Replication Fork Reversal to Promote Genome Stability. *Mol. Cell* **81**, 198-211.e6 (2021).
66. Choi, E. B. *et al.* ATP-binding cassette protein ABCF1 couples transcription and genome surveillance in embryonic stem cells through low-complexity domain. *Sci. Adv.* **7**, (2021).
67. Xiao, Z. *et al.* System-wide analysis of SUMOylation dynamics in response to replication stress reveals novel small ubiquitin-like modified target proteins and acceptor lysines relevant for genome stability. *Mol. Cell. Proteomics* **14**, 1419–1434 (2015).
68. Franz, C. *et al.* MEL-28/ELYS is required for the recruitment of nucleoporins to chromatin and postmitotic nuclear pore complex assembly. *EMBO Rep.* **8**, 165–172 (2007).
69. Sarangi, P. & Zhao, X. SUMO-mediated regulation of DNA damage repair and responses. *Trends Biochem. Sci.* **40**, 233 (2015).
70. Whalen, J. M., Dhingra, N., Wei, L., Zhao, X. & Freudenreich, C. H. Relocation of Collapsed Forks to the Nuclear Pore Complex Depends on Sumoylation of DNA Repair Proteins and Permits Rad51 Association. *Cell Rep.* **31**, 107635 (2020).
71. Kuhn, T. M. & Capelson, M. cells Nuclear Pore Proteins in Regulation of Chromatin State. doi:10.3390/cells8111414.
72. Zhang, X. *et al.* Proteome-wide identification of ubiquitin interactions using UbIA-MS. *Nat. Protoc. 2018 133* **13**, 530–550 (2018).
73. Ritchie, M. E. *et al.* limma powers differential expression analyses for RNA-sequencing and microarray studies. *Nucleic Acids Res.* **43**, e47–e47 (2015).
74. De Wyn, J. *et al.* Meis2 is an adrenergic core regulatory transcription factor involved in early initiation of th-mycn-driven neuroblastoma formation. *Cancers (Basel).* **13**, (2021).

Figure 1. PHF6 interacts with RRM2 and proteins involved in nuclear transport, SUMOylation and cell cycle regulation.

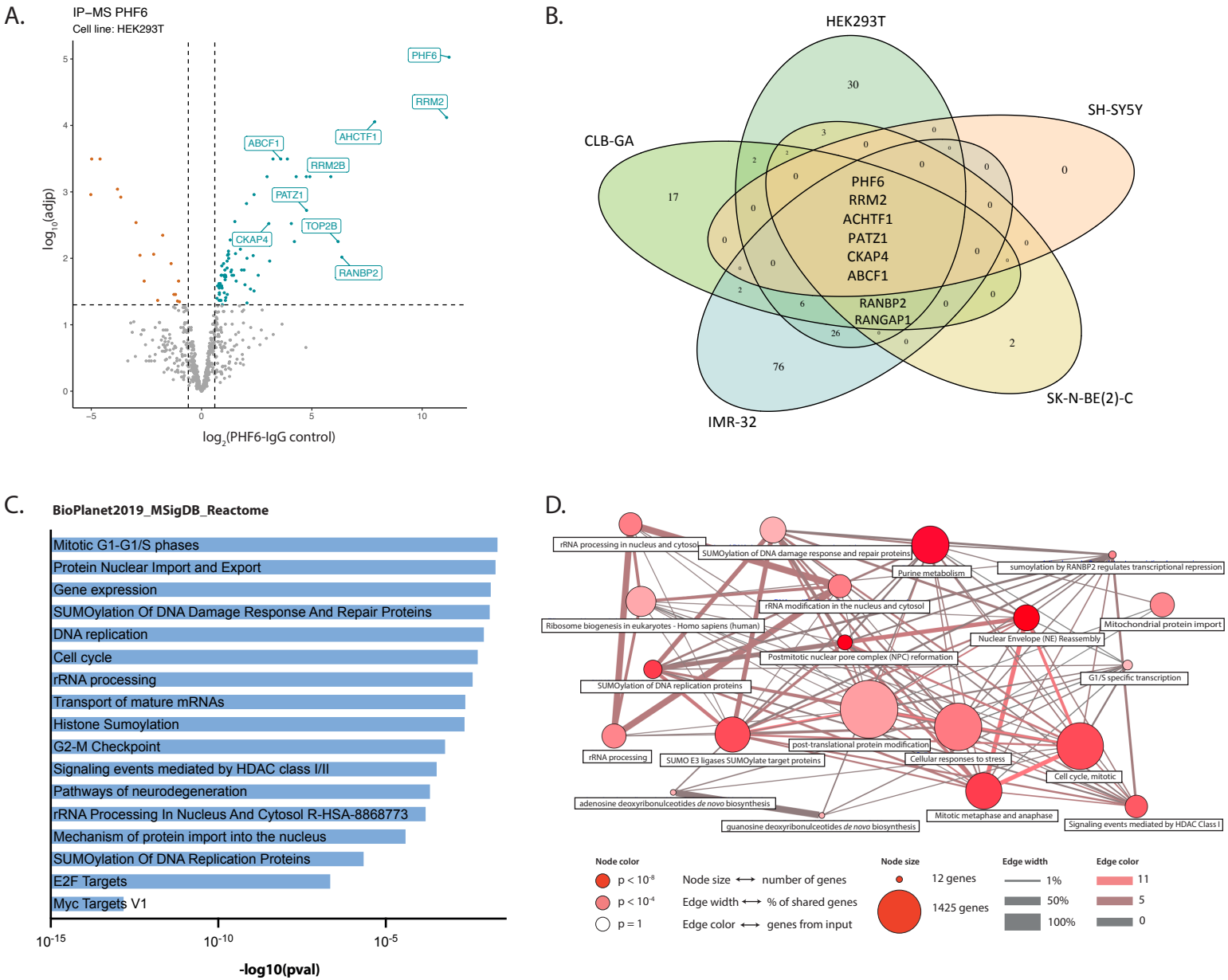

Figure 2. PHF6 interacts with RRM2 through its first PHFD domain

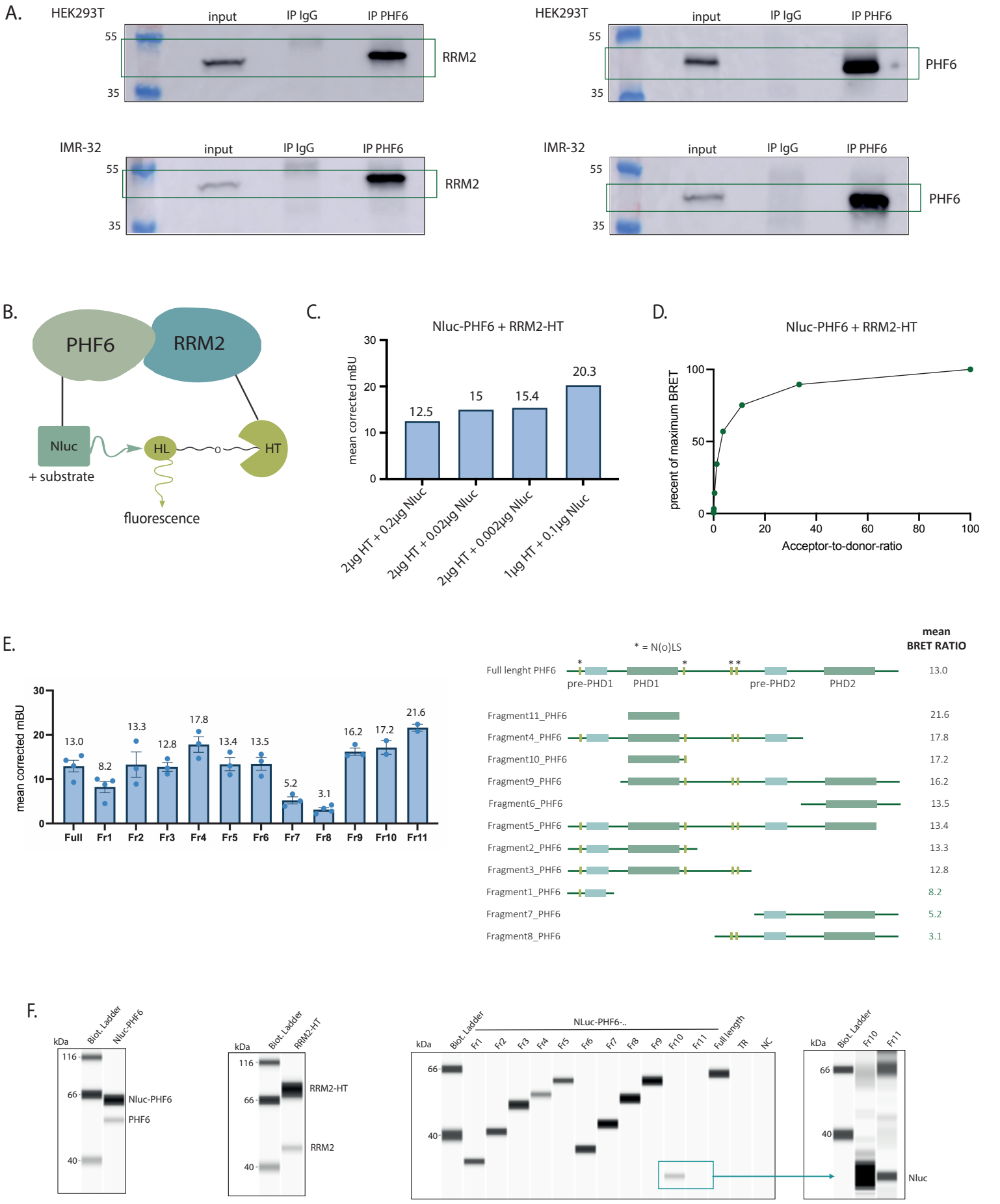

Figure 3. High *PHF6* expression is correlated with poor prognosis in primary neuroblastoma

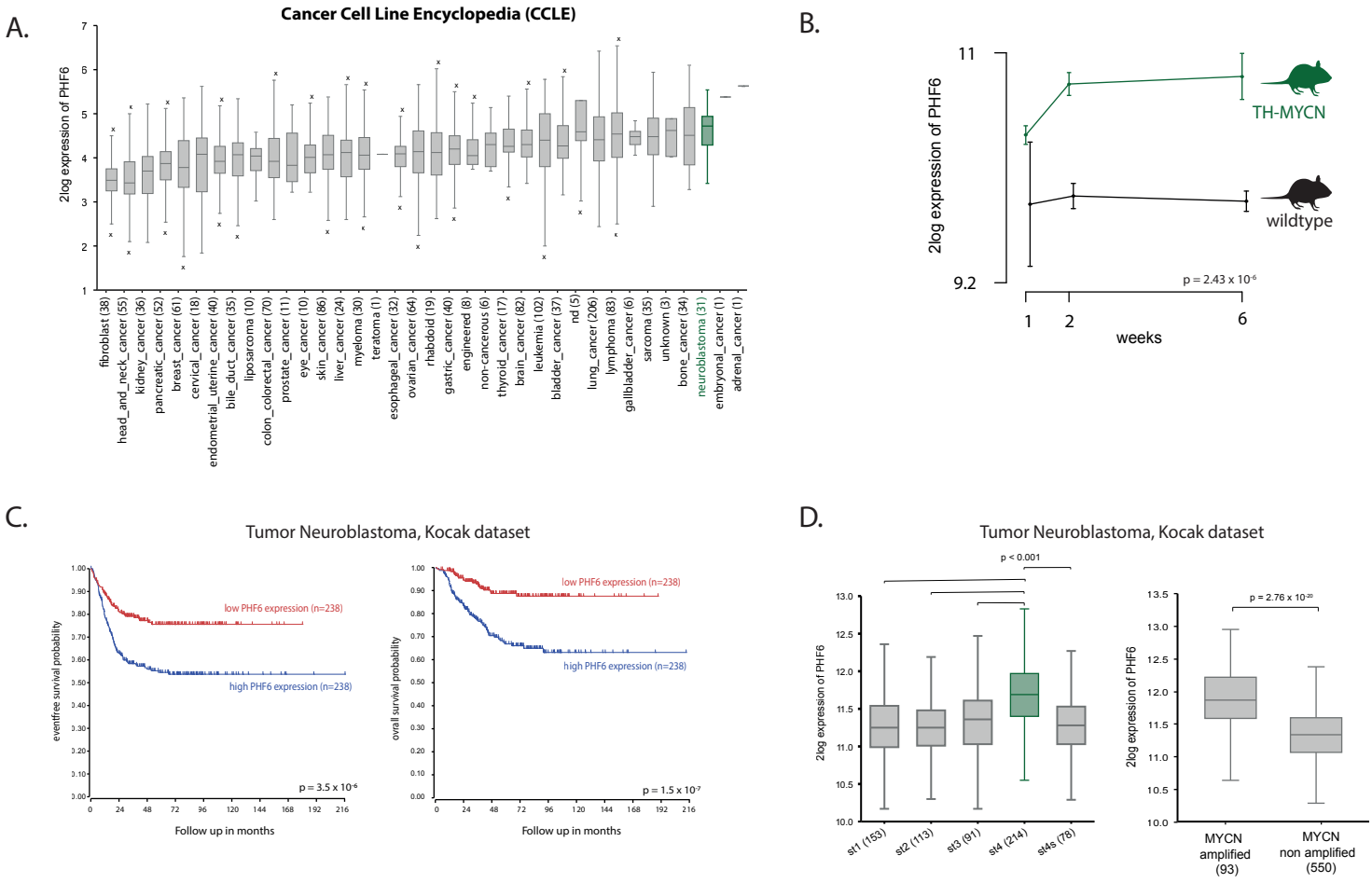

Figure 4. High *PHF6* expression as putative biomarker for pharmacological CHK1 inhibitor sensitivity

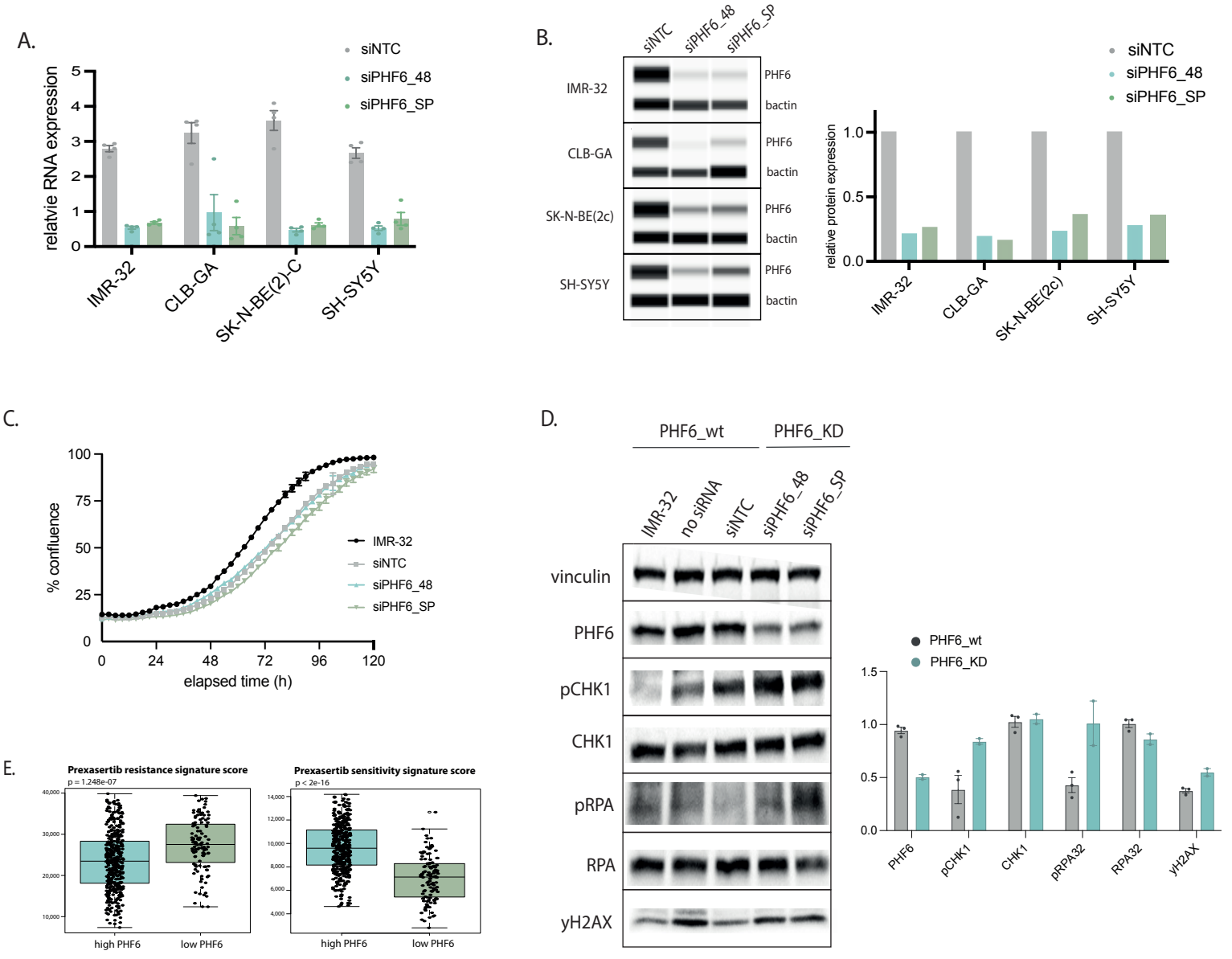

Figure 5. *PHF6* knockdown leads to downregulation of neuroblastoma CRC regulated and H3K56ac associated gene signatures

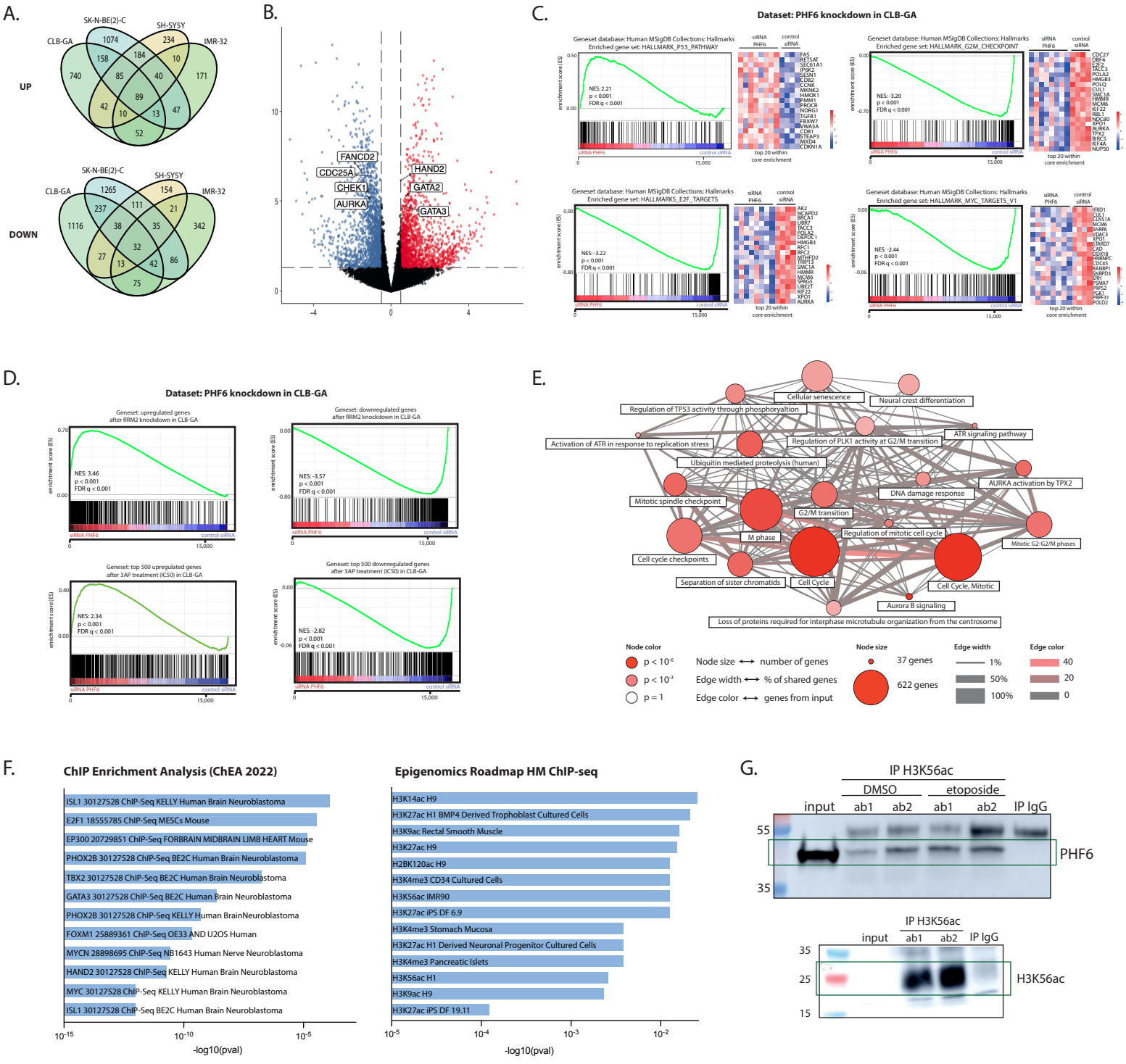

Figure 6. CUT&RUN reveals binding of PHF6 to the ADR CRC in neuroblastoma

A.

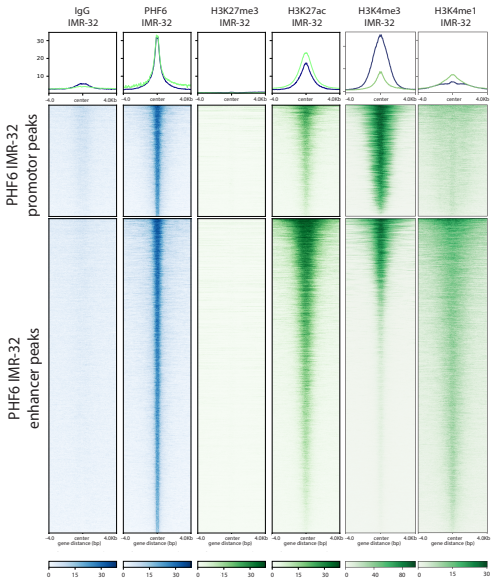

B.

Motif Name	Consensus	p-value
Ascl1 (bHLH)		1×10^{-379}
Phox2a		1×10^{-326}
CTCF		1×10^{-317}
Isl1		1×10^{-250}
Phox2b		1×10^{-175}
Hand2		1×10^{-104}
Gata3		1×10^{-78}
Gata2		1×10^{-71}
Meis1		1×10^{-67}

C.

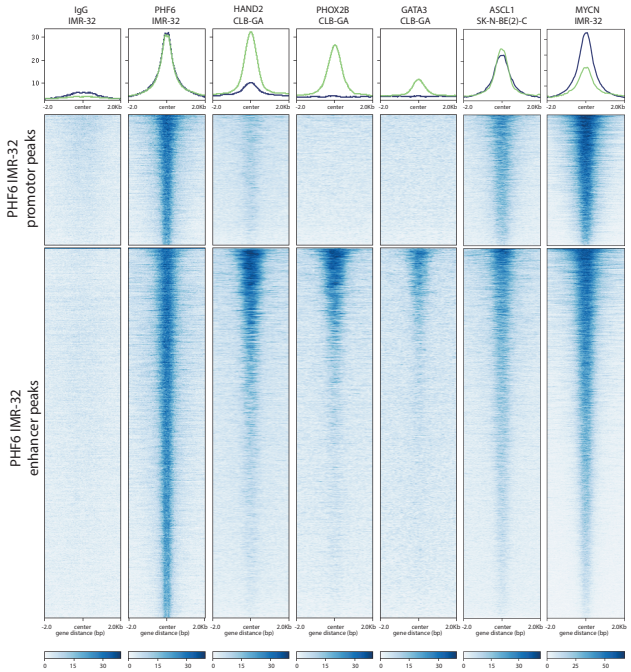

D.

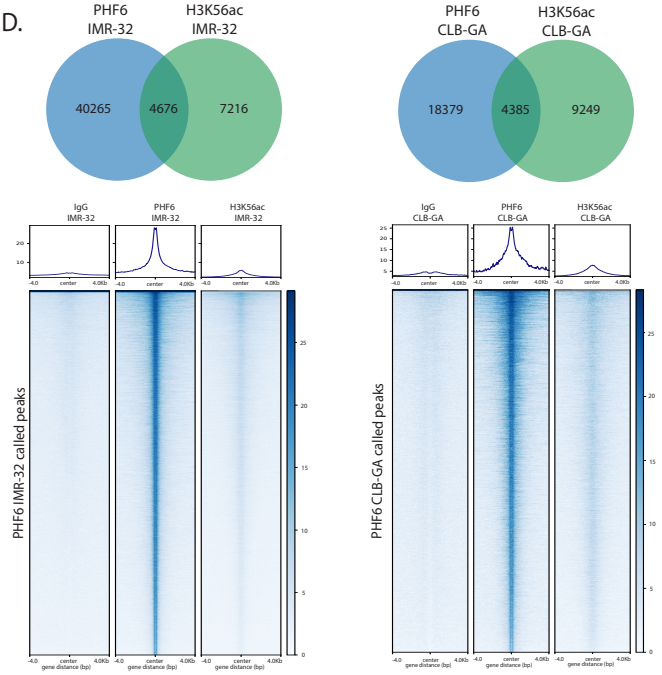

E.

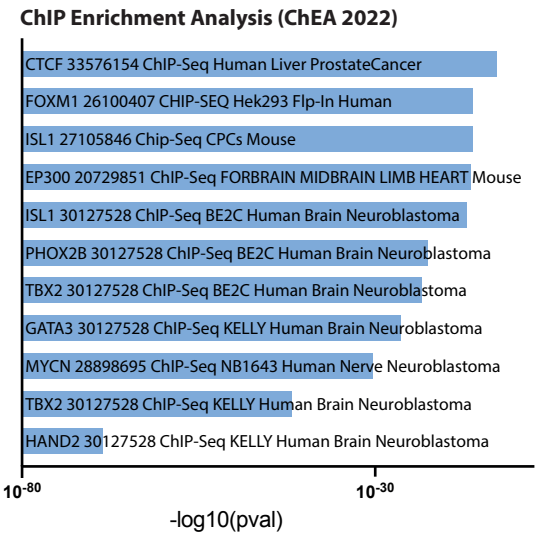
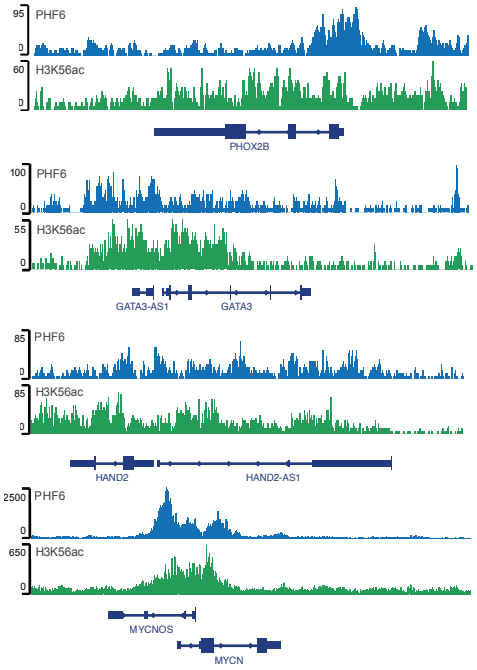
F.